LAWRENCE
LIVERMORE
NATIONAL
LABORATORY

LLNL-JRNL-665254

Developing a bright 17 keV x-ray source for probing high-energy-density states of matter at high spatial resolution

C. M. Huntington, H. S. Park, B. R. Maddox, M. A. Barrios, R. Benedetti, D. G. Braun, C. E. Wehrenberg, B. A. Remington, S. P. Regan

December 11, 2014

Physics of Plasmas

Disclaimer

This document was prepared as an account of work sponsored by an agency of the United States government. Neither the United States government nor Lawrence Livermore National Security, LLC, nor any of their employees makes any warranty, expressed or implied, or assumes any legal liability or responsibility for the accuracy, completeness, or usefulness of any information, apparatus, product, or process disclosed, or represents that its use would not infringe privately owned rights. Reference herein to any specific commercial product, process, or service by trade name, trademark, manufacturer, or otherwise does not necessarily constitute or imply its endorsement, recommendation, or favoring by the United States government or Lawrence Livermore National Security, LLC. The views and opinions of authors expressed herein do not necessarily state or reflect those of the United States government or Lawrence Livermore National Security, LLC, and shall not be used for advertising or product endorsement purposes.

Developing a bright 17 keV x-ray source for probing high-energy-density states of matter at high spatial resolution

C. M. Huntington, H.-S. Park, B. R. Maddox, M. A. Barrios, R. Benedetti, D. G. Braun, C. E. Wehrenberg, and B. A. Remington
LLNL

M. Hohenberger and S. P. Regan
LLE

A set of experiments was performed on the National Ignition Facility to develop and optimize a bright, 17 keV x-ray backlighter probe using laser-irradiated Nb foils. High-resolution one-dimensional imaging was achieved using a 15 μm wide slit in a Ta substrate to aperture the Nb He$_\alpha$ x-rays onto an open-aperture, time integrated camera. To optimize the x-ray source for imaging applications, the effect of laser pulse shape and spatial profile on the target were investigated. Two laser pulse shapes were used– a "prepulse" shape that included a 3 ns, low-intensity laser foot preceding the high-energy 2 ns square main laser drive, and a pulse without the laser foot. The laser spatial profile was varied by the use of continuous phase plates (CPPs) on a pair of shots, while beams were arrayed at best focus without CPPs. A shared set of comprehensive diagnostics allowed for a direct comparison of several figures of merit, including imaging resolution, total x-ray conversion efficiency, and x-ray spectrum. The use of CPPs was seen to reduce the high-energy tail of the x-ray spectrum, which was unaffected by the laser pulse shape. The imaging resolution measured was comparably high for all combinations of laser parameters, but a higher x-ray flux was achieved without phase plates. This is a direct result of the increased flexibility in laser pointing from smaller laser spot sizes, allowing the laser energy to be delivered to the Nb foil aligned in a way that maximizes the resulting x-ray flux that passes through the slit aperture and reaches the imaging detector. This is the first demonstration of point-projection geometry imaging at NIF at the energies (>10 keV) necessary for imaging denser, higher-Z targets than have previously been measured.

The need for x-ray sources for use as diagnostic probes of internal confinement fusion (ICF) and high-energy-density (HED) experiments on the National Ignition Facility (NIF) is well-established [1–7]. The x-rays are the result of laser-illumination of a thin metallic foil or metal-doped foam, where atomic transitions between energy levels–generally the $1s2 - 1s2p$ He$_\alpha$ transition in the ionized atom–generate the characteristic radiation. Such probes are often used to backlight a sample of interest, such as implosion capsules in the ICF context [8], or shock- or ramp-compressed HED samples, where the transmitted intensity contains information about the line-integrated areal density (ρR) of the sample [9]. X-ray sources are also the basis for scattering experiments[10, 11], and investigations of material properties through Bragg or Laue diffraction [12, 13], though the optimum characteristics of the x-ray probe for these applications can differ from those needed for radiography.

Important properties of x-ray sources include total x-ray yield into 4π steradians [14–16], the duration of x-ray emission [17], maximum photon energy [18], and emission source size [1, 19]. This latter condition is imposed to meet requirements for use in point-projection imaging, where the x-ray source size dictates the effective spatial resolution of the an imaging diagnostic. In this work, the application for which these experiments were being conducted requires an x-ray source with energy greater than 15 keV, and sufficiently small in extent in one dimension (1D) for imaging of features down to approximately 30 μm. These requirements were the basis for the selection of the materials used in the target, the design of the target, and the laser parameters investigated in the set of four shots reported here.

Each of the four targets in the set of experiments was effectively identical: the x-ray emitting element was chosen to be Nb, with characteristic He$_\alpha$ x-ray lines at 17.0 and 17.2 keV. The Nb foil was 12 μm thick and 1.2 mm $\times$0.6 mm in extent. The collimation of the x-ray emission was achieved using a Ta substrate, which was 5 mm $\times$ 5 mm $\times$ 100 μm-thick and served to block the x-ray emission (transmission of 17 keV x-rays is 1×10^{-7}), except at the central 15 μm $\times$ 800 μm laser-machined slot. The Nb foil was centered over the slit, and the lateral dimensions were chosen to overfill the projection of the slit along the diagnostic line of sight. To reduce the interaction of hot electrons generated during the laser pulse

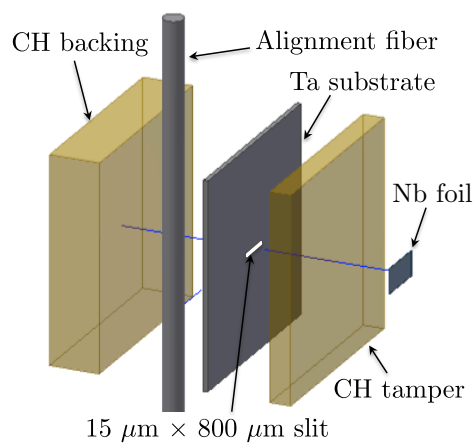

FIG. 1. The x-ray source target for all four shots, shown deconstructed along the imaging axis (indicated by the blue line). The laser drive was incident from the right, onto the 12 μm-thick Nb foil. Slit aperture enlarged for clarity and not shown to scale.

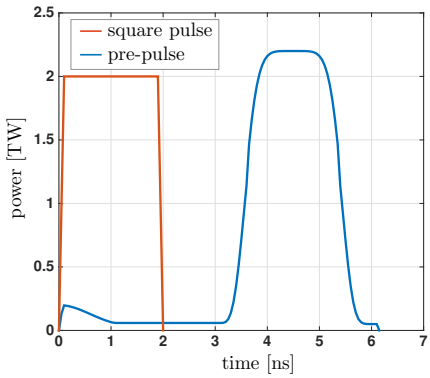

FIG. 2. Laser pulse shapes used in the experiment. The prepulse shape has a 3 ns, low-intensity foot prior to the high intensity, 2 ns square main pulse. The specific shape was chosen for comparison to previous work [2].

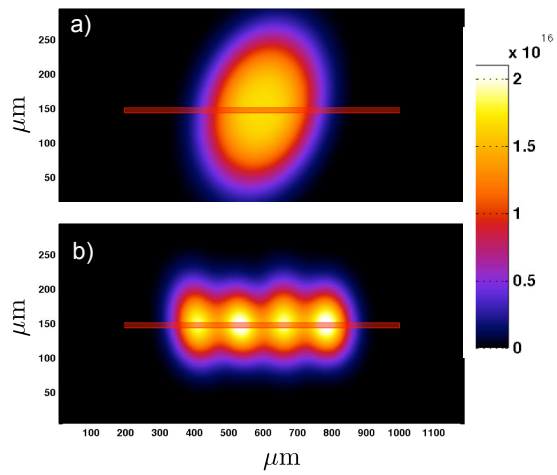

FIG. 3. Approximate laser spatial profile on target. Each shot used eight beams, pointed to a single position with 400 μm phase plates (a), and pointed to four positions in the case without phase plates (b). The projection of the slit in the Ta is indicated by the red outline in both images.

with the Ta, the substrate was sandwiched between two layers of plastic (CH), 0.5 mm thick on the laser side and 1.2 mm thick on the face directed toward the imaging diagnostic. The x-ray source target is shown in Fig. 1.

The parameters of the laser pulse used to heat the Nb foil were chosen based on the desired properties of this backlighter. Specifically, the goal was to generate an x-ray source that was efficient at producing the He$_\alpha$ lines of Nb with a proportionally low background at higher energies. One method reported in recent experiments [2, 20, 21] and simulations [22] to increase He$_\alpha$ generation is to use a laser "prepulse" of laser energy incident on the target prior to the peak in laser power. This initial phase of the laser pulse has lower intensity–10% of the main pulse intensity–and is designed to ablate material from the solid foil and generate an extended plasma plume in advance of the main pulse. The higher intensity portion of the laser pulse then interacts with the underdense, ablated plasma. The laser pulse heats and ionizes the low-density plasma, primarily through inverse Bremsstrahlung to the charge states required to produced He$_\alpha$ emission. However, the total x-ray emission is proportional to the square of the density ($\propto \rho^2$), so the decreased density in the pre-expanded blowoff region may not result in a higher overall x-ray flux [22]. For this set of experiments, two laser pulse shapes were used, as shown in Fig. 2. In both cases 8 beams were used, with a peak power of approximately 17 TW during the main 2 ns square drive. Testing the efficacy of the prepulse was one of the laser variables investigated in this set of experiments. In addition to the laser temporal shape, the spatial profile of the laser intensity on target also plays a role in x-ray generation. Experimentally, the laser profile can be tailored using continuous phase plates (CPPs), which serve to produce a more uniform laser profile [23]. This is desirable, as local "hot spots" in the laser profile can reach intensities where hot electron generation is more pronounced. These suprathermal particles may interact with the Ta substrate and generate Ta K$_\alpha$ emission near 57 keV, which manifests as a background signal in our imaging diagnostic. Testing the spectral content (i.e. intensity of background) from experiments with and without CPPs was one of the goals for this experiment.

As the atomic number of the emitting element increases, so does the intensity needed to optimize the efficiency of x-ray generation [2, 24, 25]. At this time an intensity optimization has not been conduced for Nb, though comparison with Zr experiments indicate that the optimum intensity is $>1\times10^{15}$ W/cm^2 with a prepulse [2], and comparison with Ge suggests that an optimum is $>3\times10^{15}$ W/cm^2 without a prepulse [24]. For a fixed beam energy (approximately 4 kJ per beam) and laser pulse (Fig. 2), the laser intensity in the experiment is determined by the spot size. The smallest spot size currently available from CPPs on the NIF is 400 μm diameter. In experiments when the CPPs were used, all beams were overlapped and the intensity on target was 1.7×10^{16} W/cm^2 [Fig. 3 a)].

Nearly the same intensity can be achieved using one beam at best focus, approximately 150 μm diameter, generating a peak intensity at 1.2×10^{16} W/cm^2. To assess the effectiveness of a line-source of 8 individually pointed spots, 2D simulations were run with the radiative-hydrodynamics code Lasnex [26]. The x-ray strength at a particular energy and along a given line of sight is obtained by taking a line integral of the emission and absorption from the simulation. Additionally, slicing using a plane perpendicular to the plane of the Nb foil gives the spatial distribution of emission on the driven side of the Nb foil. This is shown in Fig. 4 a) for a single beam, without a prepulse, and incident from the bottom at 50° to the Nb foil normal. The beam is indicated by the arrow, and the colormap shows the integrated emission at 17.2 keV in the vertical plane perpendicular to the Nb foil surface.

Under single-beam illumination the peak in x-ray emission is initially located behind (aligned with), the imaging slit. After 1 ns of laser illumination, the brightest emitting region (approximately the critical density surface, n_{crit}) begins to recede into the target, translated along the beam axis. The

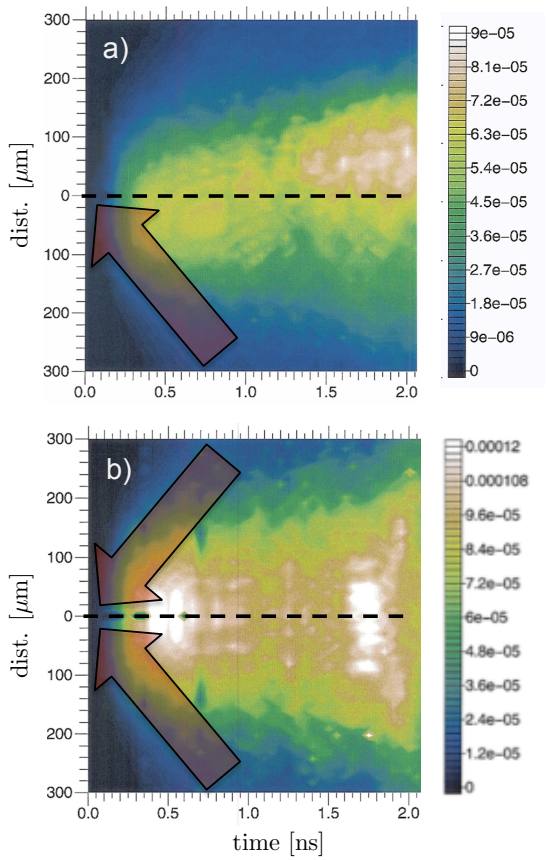

FIG. 4. Simulations of line integrated x-ray emission at 17.2 keV from (a) asymmetric, one-beam illumination, and (b) symmetric, two-beam illumination of the Nb foil. Both cases shown are the without-prepulse laser pulse shape. The slit is centered at 0 μm and indicated by the dashed line in both figures. Arrows represent approximate incoming angle of lasers beams. The region of greatest emission is seen to move off of the slit axis when the foil is driven asymmetrically.

50° beam incidence angle means that n_{crit} also moves off of the central axis, and is located 50 μm above the slit axis by the end of the laser pulse. This significantly decreases the x-ray flux transmitted through the 15 μm slit during the later portion of the pulse. Under symmetric illumination, however, the emitting volume remains aligned with the slit [Fig. 4 b)], ensuring that the maximum x-ray flux is transmitted to the imaging detector. Symmetric illumination was achieved by pairing beams and aligning the four foci along the slit dimension [Fig. 3b)]. This generated four spots, and without CPPs the spots had peak intensities from 2.0 – 2.2$\times 10^{16}$ W/cm^2.

The effect of both the prepulse and CPPs are evident in the data from the static x-ray imaging (SXI) diagnostic. This low-magnification (2×) time-integrated pinhole imager viewed the Nb foil at 83° to its normal, i.e. nearly edge-on to the driven foil. The camera was oriented at 71° with respect to the long axis of the slit, effectively imaging the laser spot along the length of the slit. An SXI image from each shot is shown in Fig. 5, taken from a channel that was filtered with 50 μm Ti. Accompanying the set of four images are the inte-

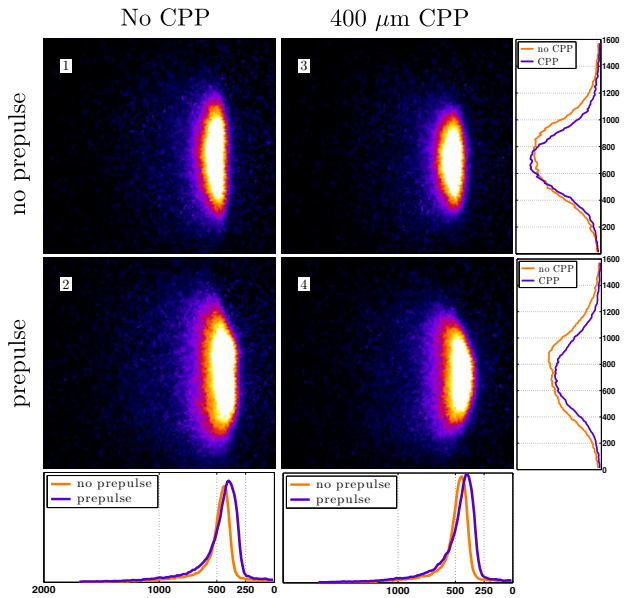

FIG. 5. Images from the static x-ray imager (SXI); the laser pulse is incident from the left in each frame, and the Ta slit (not shown) is oriented vertically in these images. Distance measurements are shown in microns, and each frame is shown on the same arbitrary intensity scale, to illustrate the difference in the x-ray emitting region as a result of the various laser parameters.

grated intensity profiles along the two axis, in arbitrary units, for comparable shots. The slit is oriented approximately vertically in the images. As shown in Fig. 3, when the eight beams without CPPs were arrayed into four spots along the slit, the emitting region was larger along the slit direction (the cases without CPPs is wider in both plots on the right-hand side of the figure). Comparing the images from shots with identical beam spatial profiles, the prepulse does generate a lager x-ray emission region, which has expanded in the lateral direction (along the slit), and away from the foil surface. It is clear from both bottom plots that when a prepulse was used, x-rays are generated deeper in the target. With CPPs, the prepulsed Nb foil emission was observed 87(±18) μm deeper; without CPPs the difference was 98 (±18)μm. This is consistent with motion of the Nb foil as a result of the prepulse, which has an intensity of $\approx 1 \times 10^{15}$ W/cm^2. [1]

The passive imaging diagnostic HEIDI was employed to

[1] With values from Ref. [27], we can calculate how far the Nb foil may have moved from the prepulse laser intensity:

$$P_{Mbar} = 40 \left(\frac{I\ [\mathrm{W/cm^2}]}{\lambda \times 10^{15}} \right)^{2/3} \approx 80(\pm 40)\mathrm{Mbar} \quad (1)$$

$$P = \rho_0 U_s U_p \quad (2)$$

$$\rho_0 = 8.59\mathrm{g/cm^3}, U_s = 4.44 + 1.21 U_p \text{ km/s} \quad (3)$$

$$P = 80(\pm 40)\mathrm{Mbar} = 8.59\mathrm{g/cm^3}(4.44 + 1.21 U_p) U_p \text{ km/s} \quad (4)$$

$$\text{solving, } U_p = 26(\pm 7)\ \mu\text{m/ns} \quad (5)$$

From this rough estimate, the Nb foil may move 78(±21) μm as a result of the 3 ns prepulse. This agrees with the measured values of 87 and 98 μm.

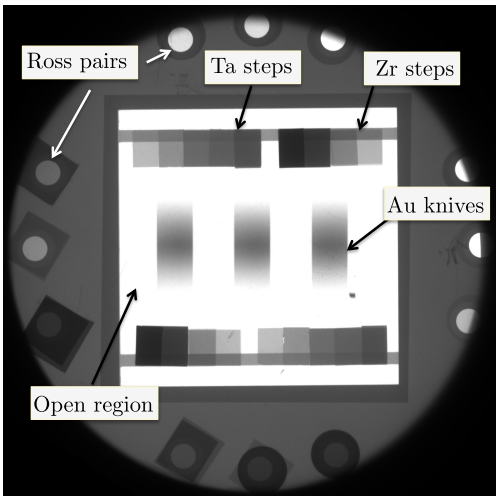

FIG. 6. An example (one of the four) image recorded from the HEIDI diagnostic. Features on the target (Au knife edges) and in the filte packs (Ross Pairs, Ta and Zr steps) are labeled.

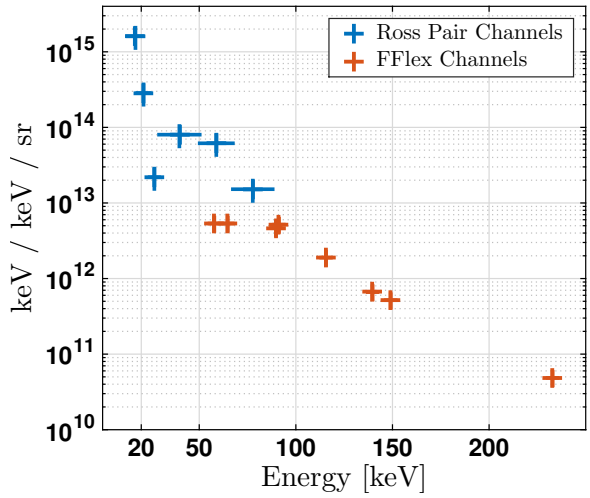

FIG. 7. Ross Pairs and FFLEX diagnostics measure the x-ray signal equal to and above the Nb He$_\alpha$ lines. Shown is the the data from the brightest shot, when a prepulse was used with lasers at best focus. The spectrum inferred from the two diagnostics is representative of the four shots, where a high-energy x-ray tail was observed to extend to greater than 200 keV for all shots.

measure the imaging characteristics of the x-ray source. The HEIDI consists of an open-apertured front end, followed by a series of filter locations and finally an SR-type image plate (IP) used to record the x-ray signal. An example image is shown in Fig. 6; each image was converted into units of photo-stimulated luminescense (PSL) and corrected for temporal fade prior to analysis [7]. Numerous diagnostic features are resolved in the image. Around the perimeter, a set of Ross pair filters provides a coarse spectrographic measurement of the x-rays reaching the IP [28]. The spectrum determined by the Ross pairs can be forward propagated through sets of step filters of various thicknesses (Ta and Zr in this case), to understand the high-energy background components of the spectrum, beyond the highest Ross pair edge. At the center of the image are a set of three, 50 μm-thick Au rectangles, which act as "knife-edge" targets to generate an approximate step function in the recorded x-ray signal. From this, the modulation transfer function (MTF) can be measured, quantifying the ability of the imaging system to record features in the target at a range of spatial scales [29].

The high-energy spectrum was measured using Ross pairs [28] and the FFLEX diagnostic [30]. The Ross pair spectral analysis shows that the x-ray emission is was dominated by the Nb He$_\alpha$ line, which was measured in the Zn and Zr Ross filter pair (9.7 - 18.0 keV). The x-ray flux decreased at higher x-ray energy for all shots; Fig. 7 shows the data from the Ross pairs and FFLEX for the shot with a laser prepulse and without CPPs. The Ross pair spectrum accounts for x-rays with sufficient energy to pass through the 100 μm thick Ta substrate, which may include Ta K$_\alpha$ emission (57.5 keV) generated by a hot electron population, though the diagnostic does not have sufficient resolution to confirm this. The absolute conversion efficiency to Nb He$_\alpha$ was measured using the first Ross pair channel, and was found to be approximately 0.1% without CPPs and up to a factor of 2 larger with CPPs. This measurement represents emission into 4π for direct comparison to the the C.E. inferred from the Super-Snout spectrometer, as presented below.

Complementing the Ross pair set, the FFLEX diagnostic was used to measure the x-ray spectrum in a series of channels from 20 - 200 keV. Assuming that the observed x-rays were produced as a result of bremsstrahlung emission from a Maxwellian electron population, the temperature and energy content of the electron population can be calculated. Summarized in Table I, the measured electron temperature in shots without CPPs was slightly lower than when CPPs were used (approximately 36 keV, versus 41 keV, respectively). However, the x-ray intensity was higher without CPPs; the total energy content in the hard x-ray component was measured to be 595 J without CPPs, compared to 230 J when the CPPs were used. This increased signal at higher energy manifests itself as a uniform background that passes through all components in these targets.

The transmission of the Ta and Zr steps can be used to further assess the energy in the x-ray spectrum, above the limits of the Ross pairs (ie. the high-energy background). By forward-propagating the measured spectrum through the steps (of known thickness), a synthetic step profile can be generated and matched to the observed values. In each case, the Ross pair spectrum is seen to accurately reproduce the ratio of measured intensities between the steps. In order to match the *absolute* values of the measured intensities, an additional background must be added. This scalar background signal is the same for both Ta and Zr steps, indicating that it is generated by x-rays above the Ta K-edge (67 keV). At energies below this, for example 57 keV Ta K$_\alpha$, x-rays would be transmitted at 75% through the thickest Ta step (50 microns) and 30% through the thickest Zr step (550 microns). However, for energies over 67 keV, these two materials have nearly the same transmission, and so x-rays above this will be recorded

at the same level on the two materials.

The high energy background level was approximately twice as high in the case without CPPs as with CPPs (2.6 PSL without CPPs vs 1.35 with CPPs, as shown in Table I). This is in agreement with the energy content measurements made with FFLEX, where approximately twice as much energy above 170 keV was inferred for the shots without CPPs. When the same spatial laser profile was used (either with or without CPPs), the background content of the shots (with and without prepulse) were equal to within measurement errors.

The spatial resolution of the imaging system was quantified using the Au "knife edge" foils, which were stood-off from the slit-projection source and imaged using the HEIDI. The 50 μm-thick foils were located 40.7 mm from the Ta substrate and 530 mm from the image plane, and thus were imaged at magnification of 14×. For each shot in the series, several MTF measurements were made by repeatedly sampling the edge spread curves at the Au edges. Differentiation produced a line spread function (LSF) for each, which was fit to a sum of two Gaussians, fully capturing the LSF shape. The fit to the data was used to generate the MTF, and the repeated measurements were averaged to produce the resolution curves shown in Fig. 8.

In slit-projection backlighting, the image resolution is largely determined by the size of the x-ray aperture, which was 15 μm in the case of the experiment described here. For these experiments, the dominant feature in the LSF is well-fit by a Gaussian with $\sigma \approx 6$ μm, as shown in Table I. The source size full-width at half-maximum (FWHM) is then $2\sqrt{2\ln(2)} \approx 14$ μm, which is consistent with the aperture width and compares well with previous measurements of point-projection and mirco-flag imaging systems [31, 32]. However, in the range of target feature sizes important for this experiment–features less than a few hundred microns–the MTF effectively asymptotes at 0.8. This is the result of a broad, low-flux x-ray signal which limits the achievable resolution and manifests in the LSF as a broad ($\sigma \approx 80$ μm, FWHM ≈250 μm), low-amplitude peak. From the fitted parameters it is estimated that this secondary source size is 200-250 μm in extent and approximately co-located with the Ta slit. This is consistent with x-ray generation from a forward-directed population of laser-driven hot electrons that traverse the CH tamper and interact with the Ta substrate, generating 57 keV Ta K_α x-rays.

The absolute conversion efficiency from laser energy to He_α x-ray energy was assessed with the Supersnout-II spectrometer (SSIIS). The SSIIS is an absolutely calibrated crystal spectrometer with energy coverage via PET crystals from 6 - 16 keV. As such, the Nb He_α line was recorded on three crystal channels in second-order. The SSIIS line-of-sight to the Nb sample was perpendicular to the foil normal (ie. edge-on to the foil), so the Ta substrate played no role in the measurement. Constraints in fielding the diagnostic limited its use to only two of the four shots, and it was only fielded on shots with a laser pre-pulse. One channel from each shot is shown in Fig. 9. From the unattenuated SSIIS view of the Nb foil, the conversion efficiency (CE) of laser energy into Nb He_α photons can be absolutely calculated. When the laser

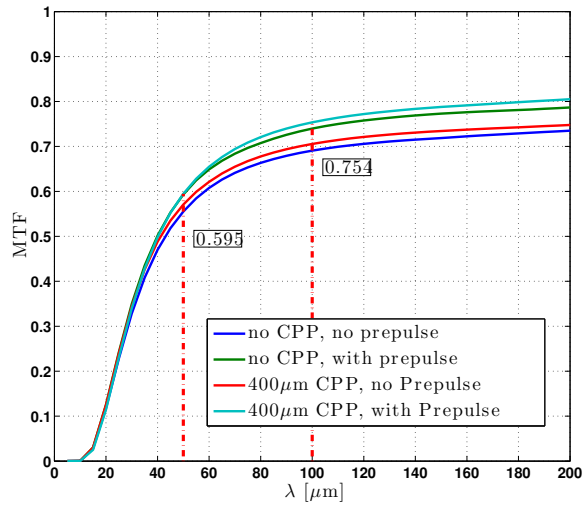

FIG. 8. Modulation transfer function curves for each x-ray source, as calculated from the edge response of the Au knife-edges. Each curve represents an average of six regions in each image–two regions on each Au sample, one from each side. The error inferred from the repeated measurement is approximately ±3% for each curve (not shown on plot for clarity).

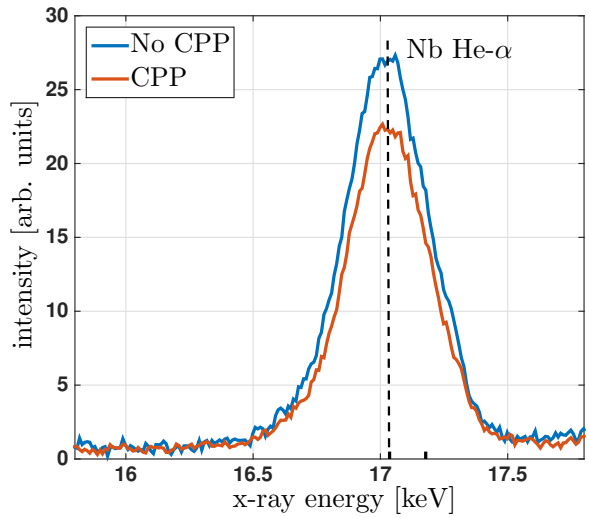

FIG. 9. Spectra collected with the SuperSnout-II diagnostic, for the pair of experiments *with* a pre-pulse. Both spectra are centered around the Nb He-like resonance line at 17.04 keV.

profile was smoothed using CPPs, the CE was measured to be 0.12 ± 0.03 % (for details of the SSIIS CE calculation, see Ref. [2] and [33]). Without CPPs, the CE was seen to increase slightly, to 0.15 ± 0.03 %. This compares well to recent studies with Mo in a similar configuration on NIF, where the CE was measured to be 0.16 ± 0.01 % using the same phase plates. The SSIIS measurements indicate that the use of CPPs does not have a significant effect on the conversion efficiency at intensities near 2×10^{16} W/cm^2.

The temporal profile of the x-ray emission was measured with the SPIDER streak camera, which approximately shares the SSII view of the Nb foil. Shown in Fig. 10, the signal

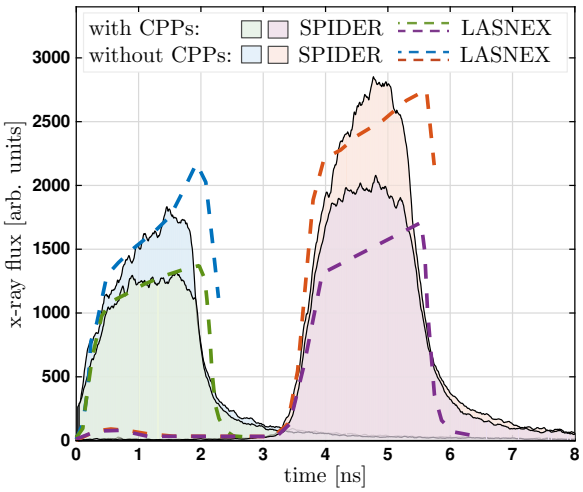

FIG. 10. Data from the SPIDER x-ray streak camera (shaded regions) and LASNEX simulations (dashed lines) for each of the four configurations. Simulations are seen to correctly predict the relative x-ray intensities and approximate temporal profile of x-ray emission.

was filtered with 10 μm of Nb, partially attenuating the signal above the Nb He$_\alpha$ line. The x-ray emission is seen to closely track the 2 TW portion of the laser profiles (Fig. 2), beginning at $t = 0$ ns for the square pulse and $t \approx 3.5$ ns for the pre-pulsed shots. The measured x-ray profile is compared with the post-processed 17.2 keV emission from LASNEX, indicated by the dashed lines in Fig. 10. Shown in scaled, arbitrary units, the simulations and data are in very good agreement: the greatest x-ray flux is generated by the pre-pulsed, non-CPP case. Generally, the emission is seen to increase when a pre-pulse is used and when the beams are at best focus, possibly due to a higher conversion efficiency to He$_\alpha$ at the higher laser intensity.

This set of four experiments provides an internally-consistent set of measurements from slit-projection backlighters fielded on the NIF. An x-ray aperture of 15 $\times$ 800 μm slit provided high spatial resolution images,with MTF >50% for 50 μm features. However, the substrate and tamper materials in the target (100 μm-thick Ta and several hundred microns of plastic) are insufficient to completely attenuate hot electrons, which generate a low-flux, high energy x-ray signal that was measured with FFLEX and Ross pairs. This hard x-ray background serves to cap the maximum MTF for wavelengths of interest (up to a few hundred microns). A laser pre-pulse improved the conversion efficiency of laser energy to He$_\alpha$ x-rays by 10 - 40%, consistent with previously measurements. However, the effective brightness at the imaging detector was increased most consistently by using a laser focus profile (without continuous phase plates) that allowed the energy to be delivered to the foil directly along the line of sight from the detector to the foil through the slit aperture. This result is consistent with 2D Lasnex simulations, and suggests a direction for future improvements to slit-projection backlighter designs.

ACKNOWLEDGMENTS

This work was performed under the auspices of the U.S. Department of Energy by Lawrence Livermore National Laboratory under Contract DE-AC52-07NA27344.

[1] O. L. Landen, D. R. Farley, S. G. Glendinning, L. M. Logory, P. M. Bell, J. A. Koch, F. D. Lee, D. K. Bradley, D. H. Kalantar, C. A. Back, and R. E. Turner, Rev. Sci. Instrum. **72**, 627 (2001).
[2] M. Barrios, K. Fournier, S. Regan, O. Landen, M. May, Y. Opachich, K. Widmann, D. Bradley, and G. Collins, High Energy Density Physics **9**, 626 (2013).
[3] J. D. Colvin, K. B. Fournier, J. Kane, S. Langer, M. J. May, and H. A. Scott, High Energy Density Physics **7**, 263 (2011).
[4] J. Workman, J. R. Fincke, G. A. Kyrala, and T. Pierce, Appl. Opt. **44**, 859 (2005).
[5] A. B. R. Cooper, M. B. Schneider, S. A. MacLaren, A. S. Moore, P. E. Young, W. W. Hsing, R. Seugling, M. E. Foord, J. D. Sain, M. J. May, R. E. Marrs, B. R. Maddox, K. Lu, K. Dodson, V. Smalyuk, P. Graham, J. M. Foster, C. A. Back, and J. F. Hund, Physics of Plasmas (1994-present) **20** (2013), http://dx.doi.org/10.1063/1.4793727.
[6] C. M. Huntington, C. M. Krauland, C. C. Kuranz, R. P. Drake, H.-S. Park, D. H. Kalantar, B. R. Maddox, B. A. Remington, and J. Kline, Review of Scientific Instruments **81**, 10E536 (2010).
[7] B. R. Maddox, H. S. Park, B. A. Remington, N. Izumi, S. Chen, C. Chen, G. Kimminau, Z. Ali, M. J. Haugh, and Q. Ma, Review of Scientific Instruments **82**, 023111 (2011).
[8] V. A. Smalyuk and et al., Phys. Rev. Lett. (in press (2014)).
[9] H.-S. Park and et al., Phys. Rev. Lett. (2014, submitted).
[10] S. H. Glenzer and R. Redmer, Rev. Mod. Phys. **81**, 1625 (2009).
[11] A. Kritcher, T. Döppner, C. Fortmann, O. Landen, R. Wallace, and S. Glenzer, High Energy Density Physics **7**, 271 (2011).
[12] B. R. Maddox, H. S. Park, B. A. Remington, C. Chen, S. Chen, S. T. Prisbrey, A. Comley, C. A. Back, C. Szabo, J. F. Seely, U. Feldman, L. T. Hudson, S. Seltzer, M. J. Haugh, and Z. Ali, Physics of Plasmas **18**, 056709 (2011).
[13] A. J. Comley, B. R. Maddox, R. E. Rudd, S. T. Prisbrey, J. A. Hawreliak, D. A. Orlikowski, S. C. Peterson, J. H. Satcher, A. J. Elsholz, H.-S. Park, B. A. Remington, N. Bazin, J. M. Foster, P. Graham, N. Park, P. A. Rosen, S. R. Rothman, A. Higginbotham, M. Suggit, and J. S. Wark, Phys. Rev. Lett. **110**, 115501 (2013).
[14] K. B. Fournier, C. Constantin, J. Poco, M. C. Miller, C. A. Back, L. J. Suter, J. Satcher, J. Davis, and J. Grun, Phys. Rev. Lett. **92**, 165005 (2004).
[15] K. B. Fournier, M. Tobin, J. F. Poco, K. Bradley, C. A. Coverdale, D. E. Beutler, T. V. III, S. B. Hansen, M. Severson, E. A. Smith, and D. L. Reeder, in *Laser-Generated, Synchrotron, and Other Laboratory X-Ray and EUV Sources, Optics, and Applications II*, 1, edited by G. A. Kyrala, J.-C. J. Gauthier, C. A. MacDonald, and A. M. Khounsary (SPIE, 2005) p. 59180N.
[16] K. B. Fournier, C. G. Constantin, J. Poco, M. C. Miller, C. A. Back, L. J. Suter, J. Satcher, J. F. Davis, and J. Grun, Laser-Generated and Other Laboratory X-Ray and EUV Sources, Optics, and Applications **5196**, 194 (2004).

Laser parameters	Shot #	Laser Intensity	SuperSnout-II	Ross Pairs		FFLEX		Step filter	Knife-edge resolution		
		$[\times 10^{16} W/cm^2]$	CE into He_α [%]	Relative signal at 17.2 keV*	CE into He_α [%]	T_e $[keV]$	E $[J]$	Background [PSL]	σ_1 [μm]	σ_2 [μm]	MTF at 50 μm
No CPPs											
square	N140214-002	2.2		0.93	0.09 (0.02)	37 (1.8)	575 (97)	2.47	6.3	91	0.56
prepulse	N140214-003	2.2	0.15 (0.03)	1	0.10 (0.03)	36 (1.6)	617 (97)	2.77	6.1	93	0.59
400 μm CPPs											
square	N140217-001	1.7		0.59	0.13 (0.03)	41 (2.1)	290 (48)	1.52	6.4	91	0.57
prepulse	N140217-002	1.7	0.12 (0.03)	0.84	0.19 (0.05)	41 (2.5)	172 (34)	1.17	6.5	90	0.59

TABLE I. Summary of the figures of merit from the diagnostic suite for each of the four shots in the Nb backlighter series. Error in calculated measurements are given in parentheses.
*Relative signal brightness is measured from the Zn / Zr channel and are corrected by the on-shot laser energy and normalized relative to the brightest case (without CPPs, with prepulse)

[17] A. B. Reighard, S. G. Glendinning, P. E. Young, W. W. Hsing, M. Foord, M. Schneider, K. Lu, T. Dittrich, R. Wallace, and C. Sorce, Review of Scientific Instruments **79** (2008), http://dx.doi.org/10.1063/1.2981173.

[18] R. Tommasini, S. P. Hatchett, D. S. Hey, C. Iglesias, N. Izumi, J. A. Koch, O. L. Landen, A. J. MacKinnon, C. Sorce, J. A. Delettrez, V. Y. Glebov, T. C. Sangster, and C. Stoeckl, Physics of Plasmas (1994-present) **18**, 056309 (2011).

[19] J. Workman, J. R. Fincke, P. Keiter, G. A. Kyrala, T. Pierce, S. Sublett, J. P. Knauer, H. Robey, B. Blue, S. G. Glendinning, and O. L. Landen, Review of Scientific Instruments **75**, 3915 (2004).

[20] F. Girard, M. Primout, D. Babonneau, J. Jadaud, M. Naudy, B. Villette, M. Miller, L. Suter, R. Kaufmann, J. Grun, and J. Davis, 32nd EPS Conference on Plasma Phys. **29** (2005).

[21] F. Girard, J. P. Jadaud, M. Naudy, B. Villette, D. Babonneau, M. Primout, M. C. Miller, R. L. Kauffman, L. J. Suter, J. Grun, and J. Davis, Physics of Plasmas **12**, 092705 (2005).

[22] D. Babonneau, M. Primout, F. Girard, J.-P. Jadaud, M. Naudy, B. Villette, S. Depierreux, C. Blancard, G. Faussurier, K. B. Fournier, L. Suter, R. Kauffman, S. Glenzer, M. C. Miller, J. Grün, and J. Davis, Physics of Plasmas **15**, 092702 (2008).

[23] Y. Lin, G. N. Lawrence, and T. J. Kessler, Opt. Lett. **20**, 764 (1995).

[24] J. Workman and G. A. Kyrala, "Scaling of x-ray k-shell sources from laser-solid interactions," (2001).

[25] J. Workman and G. A. Kyrala, Review of Scientific Instruments **72**, 678 (2001).

[26] G. B. Zimmerman and W. L. Kruer, Comments Plamsa Phys. Controlled Fusion **2**, 51 (1975).

[27] M. Meyers, *Dynamic Behavior of Materials*, A Wiley-interscience publication (Wiley, 1994).

[28] P. A. Ross, J. Opt. Soc. Am. **16**, 433 (1928).

[29] J. F. Seely, G. E. Holland, L. T. Hudson, and A. Henins, Appl. Opt. **47**, 5753 (2008).

[30] M. Hohenberger, N. E. Palmer, G. LaCaille, E. L. Dewald, L. Divol, E. J. Bond, T. Döppner, J. J. Lee, R. L. Kauffman, J. D. Salmonson, C. A. Thomas, D. K. Bradley, C. Stoeckl, and T. C. Sangster, Proc. SPIE **8850**, 88500F (2013).

[31] H. F. Robey, K. S. Budil, and B. A. Remington, Review of Scientific Instruments **68**, 792 (1997).

[32] H.-S. Park, B. R. Maddox, E. Giraldez, S. P. Hatchett, L. T. Hudson, N. Izumi, M. H. Key, S. L. Pape, A. J. MacKinnon, A. G. MacPhee, P. K. Patel, T. W. Phillips, B. A. Remington, J. F. Seely, R. Tommasini, R. Town, J. Workman, and E. Brambrink, Phys. Plasmas **15**, 072705 (2008).

[33] S. Regan, M. Barrios, K. Fournier, J. Kilkenny, J. Emig, C. Bailey, P. Bell, D. Bradley, and M. Bedzyk, .